Journal of The
Electrochemical Society

Time and Temperature Dependent Aging Mechanisms in Commercial Lithium-Ion Cells with SiO_x/Graphite Anodes

To cite this article: Jihed Ayari *et al* 2026 *J. Electrochem. Soc.* **173** 160510

Journal of The Electrochemical Society, 2026 **173** 160510

Time and Temperature Dependent Aging Mechanisms in Commercial Lithium-Ion Cells with SiO_x/Graphite Anodes

Jihed Ayari,[1,2] Mintao Wan,[1,2] Dominic Bresser,[1,2,3] and Thomas Waldmann[1,3,4,z]

[1]*Helmholtz Institute Ulm (HIU), D-89081 Ulm, Germany*
[2]*Karlsruhe Institute of Technology (KIT), D-76021 Karlsruhe, Germany*
[3]*Ulm University (UUlm), D-89069 Ulm, Germany*
[4]*Zentrum für Sonnenenergie- und Wasserstoff-Forschung Baden-Württemberg (ZSW), D-89081 Ulm, Germany*

This work addresses the limited understanding of how changes in SiO_x/graphite anodes and the N/P ratio induced by aging influence the temperature-dependent transition between degradation mechanisms. It provides insight into the potentially evolving risk of lithium plating and its implications for the safe and durable operation of batteries. Commercial 3.5 Ah Li-ion 18 650 cells with SiO_x/graphite anodes (∼2.5 wt.% Si) and Ni-rich $LiNi_{1-x-y}Mn_xCo_yO_2$ cathodes were systematically aged in the temperature range from −10 °C to +45 °C at 0.5 C and 0.85 C. Aging rates were evaluated at both beginning-of-life, i.e. 100%–95% state-of-health and mid-of-life (92.5%–87.5% state-of-health) using Arrhenius plots. The *V*-shaped Arrhenius plots at beginning-of-life exhibited minima, while the minima of the mid-of-life aged cells were either shifted to higher temperatures or even vanished in the investigated temperature range, indicating an increased susceptibility to lithium plating in the aged cells. Post-mortem analyses using FIB-SEM/EDX mapping revealed that SiO_x degradation and related side reactions are more pronounced at high temperatures, while most likely lithium plating predominates at low temperatures. Loss of anode active material in the form of SiO_x degradation and the resulting decrease in the N/P ratio is most likely the cause of the observed changes in the Arrhenius plots after cycling.

[DOI: 10.1149/1945-7111/ae959d]

Manuscript submitted June 10, 2026; revised manuscript received July 10, 2026. Published August 20, 2026.

Lithium-ion batteries (LIBs) have become an essential part of modern life, powering a wide range of devices, from small consumer electronics such as smartphones, tablet computers, power tools, as well as garden tools, to large systems powering drivetrains of battery electric vehicles and stationary energy storage for grid stabilization.[1]

An important factor in conserving resources and ensuring sustainability is a long battery life. LIBs degrade during usage, due to aging mechanisms on the material, electrode, and cell level.[2–13] In order to increase battery life, it is necessary to understand these aging mechanisms. Besides a variety of side reactions, such as transition metal dissolution from the cathode and migration to the anode,[3,6,14–17] adhesion loss,[3,18] electrode deformation,[19–23] or gas formation,[6,24–26] different studies have shown that in state-of-the-art LIB cells, the main aging mechanism is often located on the anode side.[4,5,7,8,15,27–30] While a variety of (often minor) aging mechanisms always happen in parallel, the main aging mechanisms are directly connected to the amount of cyclable Li.[15,27] The main cause of capacity fade is often found in film formation on the anode where Li is irreversibly bound, e.g. in form of solid electrolyte interphase (SEI) growth[3,4,6,13,15,31–34] or Li deposition[5,7,8,18,29–40] and film formation on its surface as well as formation of electrically disconnected "dead Li". These main mechanisms cause loss of lithium inventory (LLI) which is directly connected to the cell capacity by Faraday's 1st law.[15]

A measure for aging on the cell level is the aging rate, which can be determined from the slope of the capacity-based state-of-health (SOH) as a function of time[8,10–12,41] or cycles.[29,30,32,33,40] The aging rate is connected to the temperature via the Arrhenius law[8,42]

$$r = A \exp\left(-\frac{E_a}{k_B T}\right) \quad [1]$$

where A is a pre-exponential factor, E_a is the apparent activation energy, k_B is the Boltzmann constant, and T is the absolute temperature. The aging rate often follows an Arrhenius-like behavior for aging temperatures in a certain range, i.e. lines are obtained in a $\ln(r)$ vs. $1/k_BT$ diagram which results from linearization of Eq. 1. Data points which are on a straight line in the Arrhenius plot can be considered to originate from the same main mechanism.[8,42]

For "high temperatures" (e.g. 45 °C) it is often observed that r increases with increasing temperatures according to Eq. 1.[8,10,12,15,29,30] This reflects the intuitive behavior of increased reaction rate with increased temperature.[42] Such thermally activated side reactions are SEI growth on the anode[3,4,15,31–34] and transition metal dissolution (e.g. Mn or Fe) from the cathode and diffusion/migration to the anode.[14,15,43,44]

On the other hand, "low temperatures" (e.g. 0 °C) slow down thermally activated reactions, leading to very low aging rates in calendar aging.[27,37,45] However, if charging is involved, a different aging mechanism—Li plating[5,7,8,18,29–32,36,37,39,46,47]—comes into play, which was also observed in commercial Li-ion cells.[7,8,18,29–31,37,39,46–49] Li plating becomes thermodynamically allowed, in case the anode potential decreases below 0 V vs. Li/Li^+.[5,7,39,46,50,51] The anode potential decreases during charging and this decrease is more pronounced by polarization effects at low temperatures and high charging C-rates.[5,7,8,39,46,52] Li plating can lead to high aging rates[7,8,29–32,36,37,39,47,48] and safety issues due to exothermic reactions[7,18,33,46,53–55] of Li metal with electrolyte.

Li plating can be considered as a parallel reaction to intercalation,[56] where low temperatures decrease the probability of intercalation and increase the probability of Li plating.[7] Therefore, "low temperatures" lead to an increase of the aging rate with decreasing temperature in case of Li plating resulting in an apparent negative activation energy in the Arrhenius plot.[8,29–33,36,40] While the apparent negative activation energy might seem counter intuitive, it must not be over interpreted and can simply be regarded as a measure for the temperature dependence of the aging rate according to Eq. 1, i.e. an increased aging rate with decreasing temperature, which is typical for Li plating.[8,29–33,36,40,48,57]

Apparent negative barriers are also known from physical chemistry textbooks and indicate a fast exothermic equilibrium before an irreversible reaction step, thus changing the sign in the exponent of Eq. 1.[42] Apparent negative barriers are not a real "negative barrier" in the energetic hyperplane of the reaction.[42] In case of Li plating, this equilibrium could be adsorption/desorption of electrolyte molecules

[z]E-mail: thomas.waldmann@zsw-bw.de

on the Li metal surface, before the irreversible reaction of adsorbed electrolyte molecules with metallic Li.[8]

This temperature dependent change of the aging rate leads to a *V*-shape of the Arrhenius plot for Li-ion cells.[8,29–33,36,40] Similar to Li-ion cells, we recently also observed a *V*-shape in the Arrhenius plot of aging rates for commercial Na-ion cells with Na-plating as the low temperature mechanism.[57] The minimum in the Arrhenius plot is at the transition temperature between two main aging mechanisms and corresponds to the maximum cycle life at a given C-rate.

The transition temperature in an Arrhenius plot is determined by operating conditions and details of the cell design.[8,29,30,58] Simulations by Yang and Wang[58] and experiments from our group[29,30] showed that the transition temperature shifts to higher values with higher charging C-rates and with the electrode thickness, i.e. high-power cells with rather thin anode coatings show a lower transition temperature compared to high-energy cells with thicker anode coatings.[29,30,58] Additionally, we showed that the Arrhenius plots can change also during aging.[30,32,41] Arrhenius plots for cells with graphite anodes including a Si compound also depend on the Si content as shown by Feinauer et al. for cycling aging[36] and by Bischof et al. for calendar aging[41] both using a similar set of electrodes with the same materials. Furthermore, it has been shown that certain Si compounds in Si /graphite anodes tend to degrade especially at elevated temperatures due to SEI formation on both graphite and Si-based particles.[36,41,47,59,60] For pure graphite anodes, SEI growth leads to LLI only, however, on Si/graphite anodes, the Si compound additionally leads to LLI and loss of anode active material (LAAM).[36,41,47,59,60] For instance, Zilberman et al. observed in calendar aging of commercial 18 650 cells with Si/graphite anodes that LLI plays a minor role and the main effect on capacity fade is LAAM.[60] If LAAM predominates, this can lead to a decrease of the negative-positive (N/P) ratio.[47]

Flügel et al. recently investigated the cycling aging behavior of commercial 3.5 Ah 18 650-type cells with Si/graphite anodes (containing ∼2.5 wt.-% Si) and Ni-rich cathodes.[47] New cells of this type show Li plating at 0 °C, but not at 45 °C as demonstrated by glow discharge optical emission spectroscopy (GD-OES) depth profiling.[47] For cycling at 45 °C, this cell type showed degradation of the Si compound, which was the cause for LAAM and a subsequent shift of the N/P ratio.[47] The LAAM induced N/P shift to lower values during cyclic aging at 45 °C lead to an increased susceptibility to Li plating for subsequent cyclic aging at 0 °C.[47]

However, there is still a lack of knowledge on temperature dependent aging mechanisms in LIBs involving Si compounds in the anode and their changes during aging, especially regarding temperature dependent aging behavior. Furthermore, a direct connection of Arrhenius plots from electrochemical measurements and Post-Mortem analysis is still needed in case of SiO_x/graphite anodes. A connection between changes on the cell and material level would help to unravel the aging mechanisms involving Si-based compounds in anodes.

In the present work, we addressed this question by electrochemical analysis via Arrhenius plots of aging rates and Post-Mortem analysis on the example of commercial 18 650 cells with SiO_x/graphite anode and Ni-rich cathode. The cells were systematically cycling aged between −10 °C to 45 °C with variations of the charging C-rate (0.5 C and 0.85 C). New and selected aged cells (−10 °C and 45 °C) were subject to Post-Mortem analysis and focused-ion beam (FIB), scanning electron microscopy (SEM), and energy dispersive X-ray spectroscopy (EDX) measurements to reveal the mechanistic origin of the change in temperature dependent capacity loss.

Experimental

Cyclic aging of commercial cells.—We investigated 33 high-energy commercial 18 650-type cells from LG with a nominal capacity of 3.5 Ah and a specified voltage range of 2.5 V to 4.2 V from the same production batch. The same cell type was also investigated by Flügel et al. where they were called 'type C'[47] and by Moosmann et al.[40] The cells include a double side coated SiO_x/graphite composite anode (∼2.5 wt.% Si) and a double side coated Ni-rich NMC cathode ($LiNi_{0.824}Mn_{0.052}Co_{0.124}O_2$).[47] The anode coatings had a thickness of 82 µm on each side of the Cu foil and a porosity of 19.3% ± 0.4%.[47]

Electrochemical measurements were conducted using Basytec CTS battery test systems and the cells were aged inside Espec and Vötsch temperature chambers. Charging was performed using a constant-current constant-voltage (CC-CV) protocol with the CV phase terminated at a cut-off current of 0.05 C, while discharging was conducted with a constant current (CC) protocol until the end-of-discharge voltage was reached. Two different cycling procedures were applied, each conducted on at least two cells per temperature to assure repeatability, across a temperature range from −10 °C to 45 °C (see Table I).

These conditions were chosen to investigate the effects of different C-rates and temperatures on SOH degradation as a function of cycles. The SOH was determined from the ratio of the discharge capacity at the respective cycle and capacity of the first cycle of the same cell times 100%. While beginning-of-life (BOL) is at SOH = 100%, the end-of-life (EOL) criterion is often defined at 80%. Consequently, in this study the SOH range around 90% was defined as mid-of-life (MOL). Aging rates r were determined from the slopes of the SOH as a function of cycles for BOL and MOL corresponding to the SOH range of 100% to 95% and 92.5% to 87.5% (see Fig. 1a), respectively. The aging rates were determined from the unsmoothed SOH data by fitting lines in the BOL and MOL range for each cell.

Sample preparation.—After cyclic aging, the cells selected for the Post-Mortem characterization were discharged at 0.1 C to the end-of-discharge voltage of 2.5 V at the same temperature at which they had been cyclically aged. Cell disassembly was carried out in an argon-filled glovebox (O_2 < 0.1 ppm, H_2O < 0.1 ppm). Electrodes were rinsed with dimethyl carbonate (DMC, Sigma Aldrich, Alfa Aesar), then dried under argon atmosphere followed by vacuum drying for at least 4 h each. Samples were cut from the electrode sheets and stored in the glovebox. For subsequent analysis, the samples were transferred in an airtight container to maintain chemically inert conditions and prevent exposure to ambient moisture and oxygen.

FIB-SEM/EDX analysis.—FIB-SEM/EDX measurements were conducted on anode samples from a new cell and cyclically aged cells (0.85 C, 2.5–4.2 V) at −10 °C and at 45 °C. FIB-SEM/EDX analysis was conducted using a Zeiss Crossbeam 340 with a Bruker Quantax EDX system. To preserve sample integrity and mitigate atmospheric contamination, all specimens were transported to the microscope within an argon-filled environment using a sealed SEMILAB transfer box. Cross-sectional specimens were fabricated using a Capella Focused Ion Beam (FIB) system equipped with a gallium ion source, operating at a milling current of 1.5 nA. We note that Flügel et al.[47] had used a different technique based on a broad-beam argon ion milling system to prepare the cross-sections of anodes from the same cell type which results in larger cross-sectional areas than for FIB.

Results and Discussion

Arrhenius plots from electrochemical data on cell level: Changes during aging.—Figure 1a shows the cycling aging results at a rate of 0.5 C in the voltage range of 2.5–4.2 V. The SOH decreases rapidly between +15 °C and −10 °C with decreasing temperature. In this temperature range, the SOH decline is accelerated, i.e. the aging rate at BOL is lower than at MOL. In contrast, between +25 °C and +45 °C, the SOH decline is decelerated, i.e. the aging rate at BOL is higher than at MOL. This leads to a change of the Arrhenius plot during aging from BOL to MOL in Fig. 1b.

Table I. Cycling conditions in this study.

Cycling condition	0.5 C/4.2 V	0.85 C/4.2 V
Number of cycled cells	17	16
Voltage range	2.5–4.2 V	2.5–4.2 V
C-rate (current)	0.5 C (1.75 A)	∼0.85 C (3.00 A)

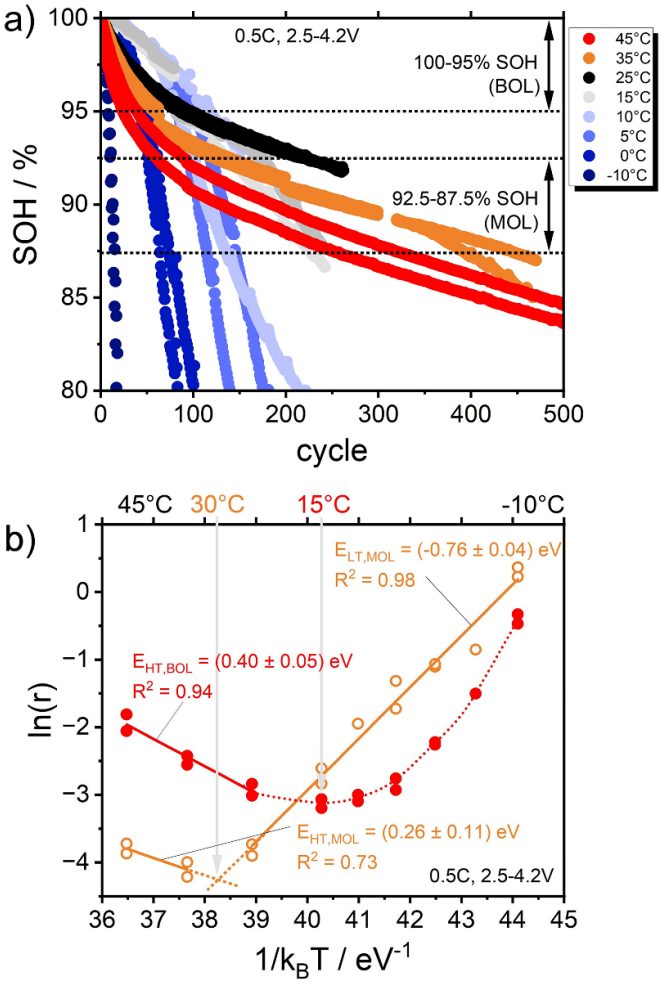

Figure 1. Cyclic aging at 0.5 C and 2.5–4.2 V in the range of −10 °C to + 45 °C. a) SOH curves as a function of cycles. The SOH regions for evaluation of the slopes for BOL and MOL are indicated. b) Arrhenius plots for BOL (red filled data points) and MOL (orange empty data points). The solid lines are linear fits. The red dotted curved line for BOL is drawn to guide the eye. The orange dotted straight lines for MOL represent extrapolations of the fitted lines to determine the transition temperature.

To derive Arrhenius plots, we analyzed the SOH degradation rates across the tested temperature range for each cyclic aging condition for BOL and MOL as indicated in Fig. 1a. The Arrhenius plots were constructed via Eq. 1.

The Arrhenius plot for BOL (red filled data points in Fig. 1b) is rather curved but linear in the high temperature (HT) range (25 °C–45 °C), similar to previous measurements with other cells[36] and in simulations.[58] The high temperature branch shows an activation barrier of $E_{HT,BOL} = (0.40 \pm 0.05)$ eV for BOL, which is comparable with values from literature of other Li-ion cell types.[8,36,41] For example, for a 1.5 Ah 18 650-type cell with graphite and NMC/LMO chemistry, a value of (0.38 ± 0.02) eV was reported for the range of 25 °C to 70 °C.[8] Bischof et al. observed activation barriers in the range of (0.29 ± 0.01) eV to (0.48 ± 0.01) eV for calendar aging at different SOCs of graphite pouch cells and (0.32 ± 0.04) eV to (0.46 ± 0.05) eV for cells with Si/graphite anodes (3% Si).[41]

The minimum of the Arrhenius plot is at 15 °C for BOL, indicating that Li plating most likely happens below this temperature, which is qualitatively consistent with other Li-ion cell types.[8,29,30,36,58] The value of the transition temperature is difficult to discuss with literature, as most data sets were not obtained from aging at a rate of 0.5 C. Kucinskis et al. aged commercial 21 700 cell type with Si/graphite anodes (86 µm anode, 30% porosity) and NCA/LNO cathodes.[30] The authors observed transition temperatures in the Arrhenius plots at ∼22.5 °C at 0.6 C and ∼20 °C at 0.4 C.[30] Therefore the transition temperature for 0.5 C is most likely in between these temperatures for those cells. In the present study, the anode coating thickness of 82 µm is comparable to the cells investigated by Kucinskis et al.,[30] however, the porosity of 19.3% ± 0.4% is lower.[47] This might explain why the observed transition temperature of 15 °C at 0.5 C is lower compared to the expected value by Kucinskis et al. (between ∼20 °C and 22.5 °C[30]). It must not be neglected that other materials, such as the separator and electrolyte might also have an influence. However, this is out of scope of the present paper.

For MOL, the Arrhenius plot is rather linear in both the high and low temperature (LT) branch with $E_{HT,MOL} = (0.26 \pm 0.11)$ eV and $E_{LT,MOL} = (-0.76 \pm 0.04)$ eV. We note that the negative value for $E_{LT,MOL}$ is also consistent with literature.[7,8,29,30,36,58,61] The minimum of the Arrhenius plot has shifted from 15 °C for BOL to 30 °C for MOL, indicating that Li plating happens below this temperature. This means that at MOL, Li plating most likely happens up to higher temperatures than for BOL, i.e. the cells may get more prone to Li plating during aging. An increase of the transition temperature in the Arrhenius plot during cyclic aging was also observed by Kucinskis et al. for 5 Ah 21 700 cells.[30] On the other hand, the lines for BOL and MOL in the Arrhenius plot in Fig. 1b cross each other at 18 °C, which means that the aging rate at MOL is lower than at BOL above this temperature.

Kucinskis et al. had pointed out, that capacity fade can be accelerated, decelerated, or linear, leading to changes in the Arrhenius plot during aging for the first two cases.[30] An example, where such a change of the Arrhenius plot during aging was not observed was shown by Gerosa et al. because the capacity fade was linear for all investigated aging temperatures from 0 °C to 45 °C for a commercial cell with graphite anode at 0.3 C.[33]

Figure 2a shows the cycling aging results at a rate of 0.85 C in the voltage range of 2.5–4.2 V. The SOH decrease for this condition shows a stronger tendency to acceleration than at 0.5 C (Fig. 1a). This leads to a different Arrhenius plot as for 0.5 C (Fig. 1b). For BOL, the minimum of the Arrhenius plot shifts from 15 °C (0.5 C, Fig. 1b) to 19 °C (0.85 C, Fig. 2b) which is consistent with previous simulations[58] and experimental results on Arrhenius plots with other cell types,[29,30] as well as with the general trend that the susceptibility to Li plating is increased at higher charging C-rate.[7,39,48] For example, Burns et al. showed for a different cell type at 12 °C that Li deposition is absent at a charging rate of 0.2 C, local Li deposition starts in small amounts at 0.5 C, and large amounts of Li plating are observed at 1 C.[48] At 50 °C, the authors showed that the onset of Li deposition happens at a charging rate of ⩾2 C.[48]

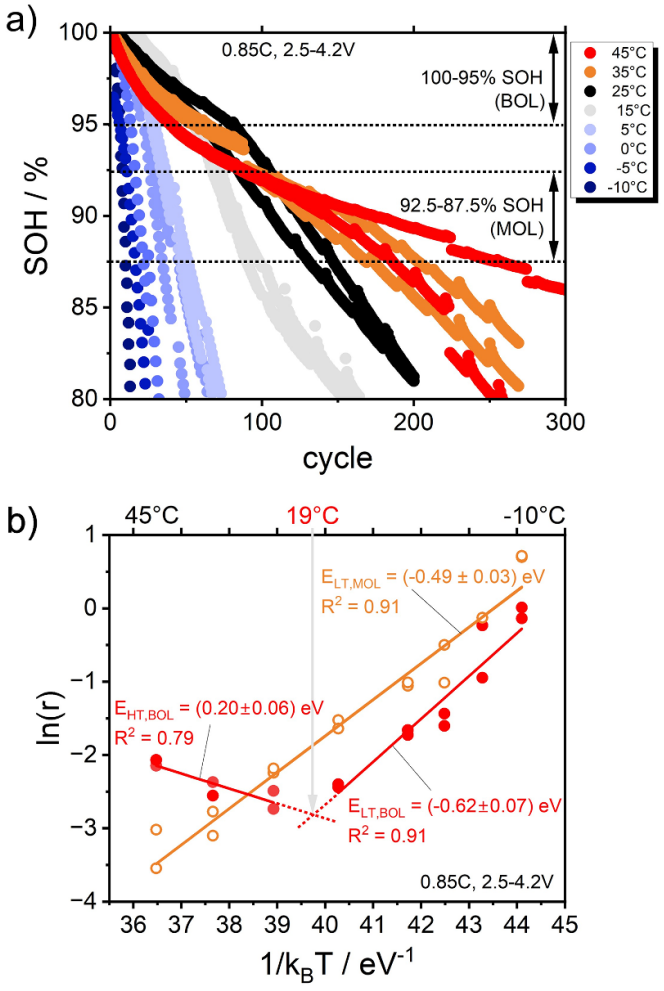

Figure 2. Cyclic aging at 0.85 C and 2.5–4.2 V in the range of −10 °C to + 45 °C. a) SOH curves as a function of cycles. The SOH regions for evaluation of the slopes for BOL and MOL are indicated. b) Arrhenius plots for BOL (red filled data points) and MOL (orange empty data points). The solid lines are linear fits. The dotted straight red lines for MOL represent extrapolations of the fitted lines to determine the transition temperature.

The change in the Arrhenius plot from BOL to MOL in Fig. 2b for 0.85 C is significantly different than for 0.5 C. While the Arrhenius plot for 0.5 C showed a clear minimum for MOL at 30 °C (Fig. 1b), there is no minimum for MOL at 0.85 C up to 45 °C. We note that there could theoretically be a minimum beyond the maximum tested temperature, i.e. >45 °C. The negative value of $E_{LT,MOL}$ = (−0.49 ± 0.03) eV indicates that Li deposition happens most likely in the whole tested temperature range of −10 °C to + 45 °C.[7,8,29,30,36,58,61]

This is fully consistent with the results by Flügel et al.[47] who aged the same cell type as in the present study (there called "type C") under the same conditions as the data points at 0 °C and at 45 °C in Fig. 2. The authors found Li plating by GD-OES depth profiling at 0 °C and degradation of the Si compound at 45 °C by GD-OES and SEM.[47] By reconstruction of anodes from new (SOH = 100%) and aged cells (SOH = 80%) into coin cells, a decrease of the anode areal capacity indicated that the Si compound in the anode lost a large part of its electrochemical activity in the aged cell and the potential curve is similar to that of graphite.[47] The similar values of remaining anode capacity in the half cell (81%) and in the original full cell (80%) as well as differential voltage analysis (DVA) indicated LAAM.[47] The degradation of the anode during aging explains the results from Fig. 2b for 0.85 C and for 0.5 C in Fig. 1b and suggests that the Si compound is degrading during cyclic aging.

FIB-SEM/EDX analysis.—To further investigate the aging mechanisms leading to the changes in the Arrhenius plots, Post-Mortem analysis was performed on i) new cells and cells cyclically aged at a rate of 0.85 C ii) at 0 °C and iii) at 45 °C.

Figure 3 shows SEM and EDX measurements of FIB cross-sections of an anode from a new cell. A region of the sample including both the anode bulk (cross-section, lower part) and the anode surface (upper part) are shown in Figs. 3a–e and Figs. 3f,g–j show SEM and EDX mappings of the anode bulk around the bright particle in Fig. 3a, respectively.

In the SEM measurements in Figs. 3a and 3f some particles appear brighter than the others which is a referring to Si-containing material. The borders of the Si-based particles appear smooth (Fig. 3f). Si particles are on both the anode surface (Fig. 3d) as well as in the anode bulk (Figs. 3d,i). These observations are consistent with the SEM observations by Flügel et al. with anodes from the same cell type.[47]

Figures 3b–e and Figs. 3g–j show EDX elemental mappings for the elements C, O, Si, and F for the same part of the sample as in Figs. 3a and 3f, respectively. In Figs. 3b and 3g, C coincides with the darker particles in Figs. 3a and 3f, which are therefore identified as graphite particles. Figures 3d and 3i shows the positions of Si containing particles, revealing that there are more of such particles than expected from the brighter appearing particles in the SEM measurement (compare Figs. 3a and 3d). At the positions of the Si-containing particles, C is mostly not present, showing that the Si particles do most likely not contain C. Others had observed Si compounds which are embedded in a C matrix[41,62,63] which is in contrast to the Si-based material in the present study.

In the previous study by Flügel et al. with anodes from the same cell type,[47] the samples were transferred through air, therefore we were not sure if this had influenced the sample. In contrast, the samples were transferred from the Ar-filled glovebox to the FIB-SEM/EDX device without air contact by a transfer chamber in the present study. Interestingly, higher O contents (Figs. 3c and 3h) coincide with those of Si, revealing the Si compound is most likely SiO_x.

The elements O (Fig. 3c) and F (Fig. 3e) are enriched on the anode surface (near the separator) compared with the cross-section which is most likely due to the initial SEI forming during cell formation. This is consistent with SEI species such as LiF, Li_2O, Li_2CO_3, and organic compounds.[64,65] A stronger SEI formation on the anode surface (i.e. near the separator) compared with the anode bulk after formation is also consistent with the surface peak in GD-OES depth profiling with anodes from the same cell type[47] and for GD-OES,[15,18,27,34,38,66–68] EELS/EDS,[69] and optical microscopy[16] measurements of anodes from other cells.

In the anode bulk (area of the FIB cross-section in Figs. 3e,j), F is found to a minor extend compared to the anode surface, mostly around both, graphite and SiO_x particles, homogeneously distributed throughout the observed samples area. This is consistent with SEI formation on the surface of the particles in the anode bulk.[64,65,70]

Figure 4 shows SEM and EDX measurements of FIB cross-sections of an anode from a cell aged at −10 °C at a rate of 0.85 C in the voltage range of 2.5–4.2 V, corresponding to the same aging conditions as for the data points for −10 °C in the Arrhenius plot in Fig. 2b.

The SEM measurements in Figs. 4a,e,j show SiO_x particles similar to those in the anode from the new cell (Figs. 3a and 3f). In contrast to the anode surface of the new cell, where the active material particles are visible, the anode surface from the cell aged at −10 °C is covered by a film, preventing the visibility of the active material particles on the surface by SEM (Fig. 4a). A deposition which is thicker than the SEI covering the active material particles is typical for Li deposition[18,34,71] which

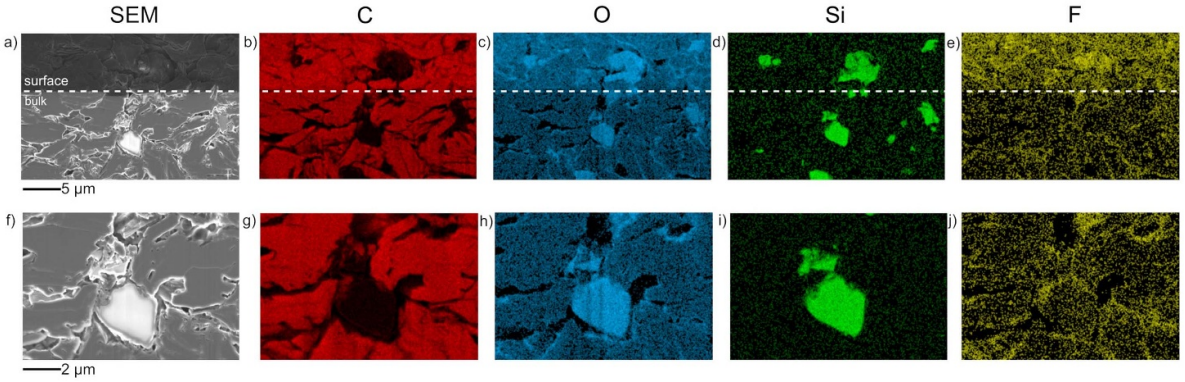

Figure 3. FIB-SEM/EDX analysis performed on an anode sample retrieved from the non-aged 18 650 cell. Observation of a–e) sample surface and cross-section (anode bulk) and f–j) cross-section around the bright particle in (a) with enhanced resolution. a) SEM and b–e) EDX mapping in the same area. f) SEM and g-j) EDX mapping in the same area.

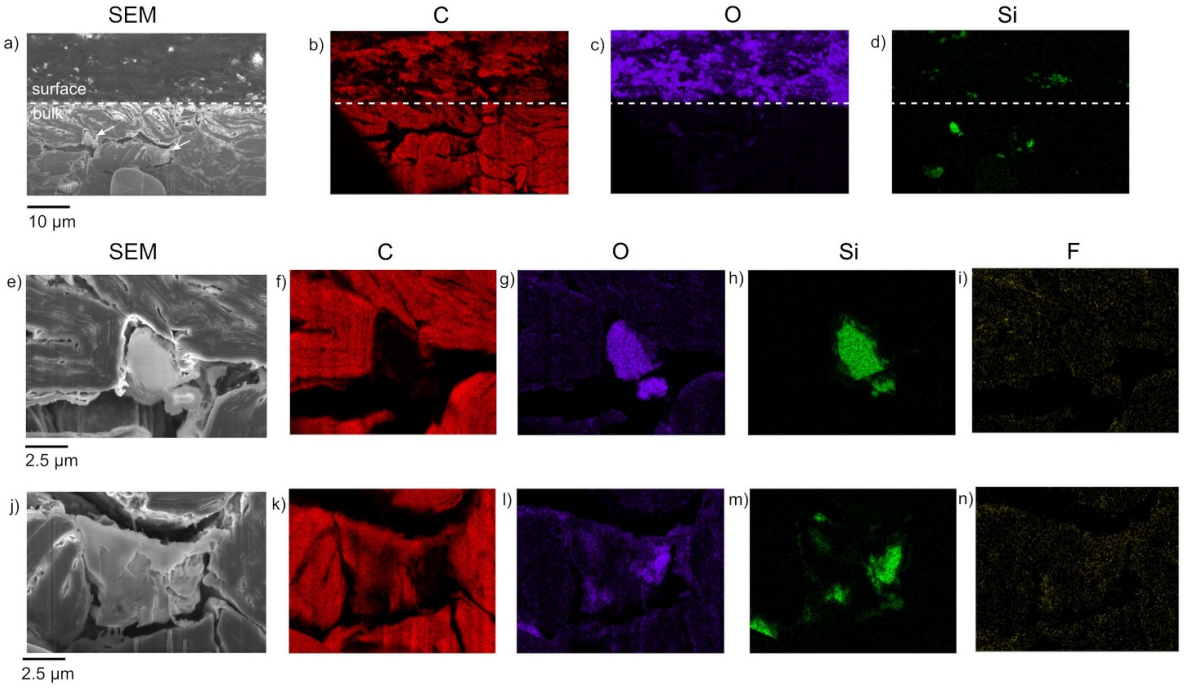

Figure 4. FIB-SEM/EDX analysis performed on an anode sample from the 18 650 cell aged at −10 °C at a rate of 0.85 C in the voltage range of 2.5–4.2 V. a) SEM measurement with anode surface and bulk. b–d) EDX measurements of the area in (a). e,f) SEM measurement of SiO_x particles marked by arrows in (a). f–i) and k–n) EDX measurements of the same areas as in e) and j), respectively.

is also supported by the Arrhenius plot in Fig. 2b and by GD-OES depth profiling measurements by Flügel et al. at 0.85 C at 0 °C.[47]

It can be seen from the EDX mapping in Fig. 4b that the intensity of C is slightly decreased on the anode surface compared with the anode bulk. The reason is that other elements are also present in the surface film such as O (Fig. 4c). We note that similarly to the anode from the new cell, O is present at the positions of Si, however, due to the overall high intensity of O on the anode surface this leads to a comparably low intensity of O in the cross-section (Fig. 4c). The coincidence of O and Si is therefore better visible in areas where only the FIB cross-section is observed (Figs. 4g,h,l,m). The exclusion of the C signal in the EDX mappings (Figs. 4f and 4k) in the presence of Si (Figs. 4h and 4m) and O (Figs. 4g and 4l) is similar in the −10 °C and the new cell (Figs. 3b–d,g–i). Similarly to the new cell, F is distributed over the surfaces of the graphite and SiO_x particles (Figs. 4i and 4n).

The borders of the SiO_x particles appear smooth after aging at −10 °C, similar to the particles in the anode from the new cell (compare Fig. 3f and Figs. 4e,j). Therefore, FIB-SEM/EDX data suggest no aging of the SiO_x particles after cyclic aging at −10 °C.

On the other hand, we find the deposition of an O-rich film on the anode surface. We underline that a chemically inert environment was ensured during cell disassembly, samples transport, and sample storage, therefore air contact is not the cause for the O signal observed on the anode surface. Although Li cannot be detected with our EDX setup, this film is rich in O (Fig. 4c), which is a hint on previously deposited Li which has reacted with carbonates from the electrolyte containing O.[34,49,61] Flügel et al. showed by GD-OES for the same cell type that Li plating is present on the anode already at 0 °C at a rate of 0.85 C.[47] Therefore, the same aging mechanism can be expected at −10 °C in this study. Li plating is also consistent with the Arrhenius plot in Fig. 2b. The preferential deposition of Li on the

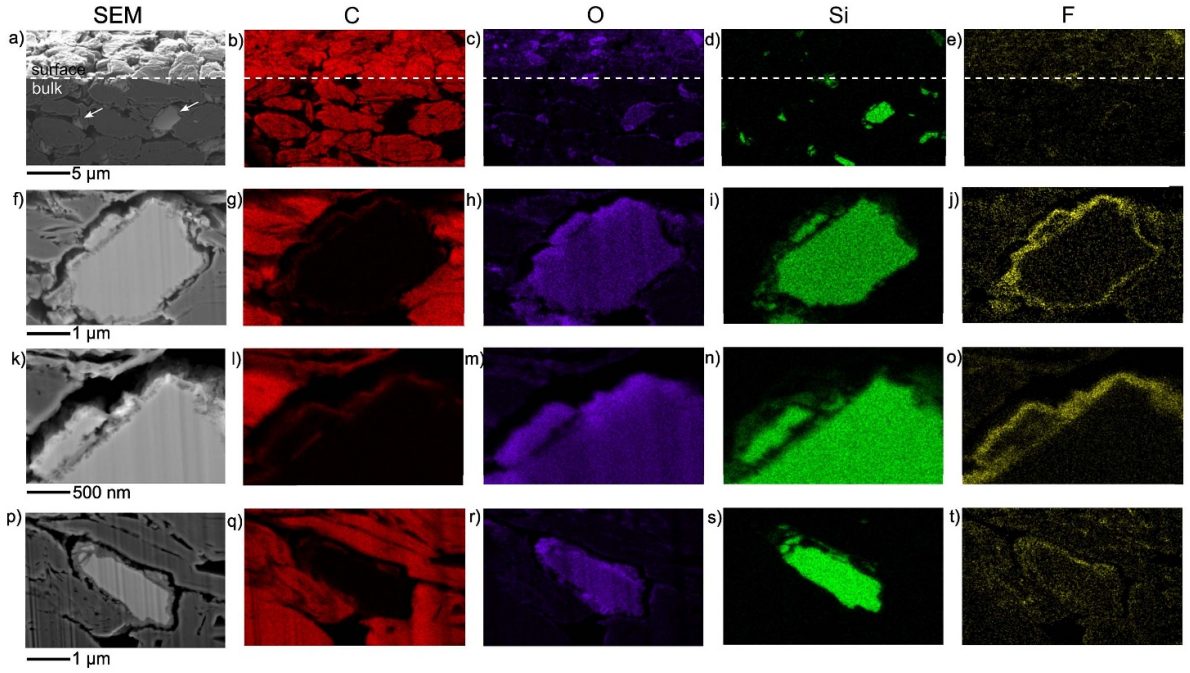

Figure 5. FIB-SEM/EDX analysis performed on an anode sample from the 18 650 cell aged at 45 °C at a rate of 0.85 C in the voltage range of 2.5–4.2 V. a) SEM measurement with anode surface and bulk. b–e) EDX measurements of the area in (a). f,k,p) SEM measurement of SiO_x particles marked in (a). g–j), l–o) and q–t) EDX measurements of the same areas as in f), k) and p), respectively. k–o) represents a zoom on the surface of the same particle shown in f–j).

anode surface (near the separator) is consistent with GD-OES depth profiling,[18,27,34,38,47,49,61,71] neutron depth profiling,[49] ^{7}Li NMR,[45] in situ optical microscopy in cross-sectioned full cells,[72] and FIB-SEM measurements,[34] as well as simulations with microstructure resolved anodes by Latz's group.[50,61,73]

The plated Li reacts with electrolyte[34,49,61] and forms electrically disconnected "dead Li",[7,61,74] both leading to LLI and to the capacity loss at low temperatures in Fig. 2a for a rate of 0.85 C and most likely also in Fig. 1a for 0.5 C. It is furthermore very likely that Li plating is the main aging mechanism for cycling aging in the voltage range of 2.5–4.2 V at a rate of 0.5 C below ∼15 °C (Fig. 1b) and at 0.85 C below ∼19 °C (Fig. 2b) for both BOL and MOL. Overall, the FIB-SEM/EDX measurements in Fig. 4 suggest no degradation of the SiO_x particles, but Li plating on the anode surface after cyclic aging at −10 °C.

Figure 5 shows SEM and EDX measurements of FIB cross-sections of an anode from a cell aged at 45 °C at a rate of 0.85 C in the voltage range of 2.5–4.2 V, corresponding to the same aging conditions as for the data points for 45 °C in the Arrhenius plot in Fig. 2b.

The SEM measurements in Figs. 5f,k,p show SiO_x particles which are not as smooth as for the anode from the new cell (Fig. 3f) and from the −10 °C aged cell (Figs. 4e,j). Instead, in Fig. 5 the SiO_x particles in the anodes from the 45 °C aged cell show a significant film formation on the SiO_x particles surfaces in SEM measurements. This is consistent with the SEM data by Flügel et al. for the same cell type[47] and for another cell type including SiO_x in the anode by Hsiao et al.[59]

The EDX mappings for C (Figs. 5b,g,l,q), for O (Figs. 5c,h,m,r), and for Si (Figs. 5d,i,n,s) are similar as for the anode from the new cell (Figs. 3b-d,g-i). In contrast to the anode from the −10 °C aged cell (Fig. 4c), we observe only a minor enrichment of O on the anode surface (Fig. 5c) after aging at 45 °C, indicating the absence of larger amounts of Li deposition at 45 °C. Here it must be considered that Li deposition at high temperatures is significantly different from Li plating at low temperatures.[7,27,34,45,75] Minor Li deposition might be consistent with GD-OES depth profiling measurements of anodes from the same cell type showing a slightly increased Li amount on the anode surface after cyclic aging at 45 °C, namely ∼0.7 wt.-% for the anode from new cell and ∼3 wt.-% for the anode from the aged cell.[47] In contrast, GD-OES measurements of anodes of the same cell type after cyclic aging at 0 °C showed a significantly higher Li amount of ∼23 wt.-% on their surface.[47]

Only minor amounts of Li deposition at MOL after cyclic aging at 45 °C are also consistent no Li deposition for BOL as indicated by the increasing aging rate in the temperature range of 19 °C–45 °C in the Arrhenius plot (red filled data points in Fig. 2b). At MOL, the main aging mechanism has changed for 45 °C, as indicated by the straight line in the Arrhenius plot (orange empty data points in Fig. 2b) showing no minimum up to 45 °C, indicating minor Li deposition. It must be considered that Li deposition most likely occurs to a minor extend at 45 °C due to higher anode potentials and if it occurs, its reaction rate with electrolyte is increased to the elevated temperature. Furthermore, we need to take into account that the aging rates of BOL and MOL cross each other in the Arrhenius plot at 29 °C (cross-section of red and orange solid lines in Fig. 2b). Therefore, the aging rate above 29 °C is lower for MOL than for BOL, even if Li deposition happens at 45 °C at MOL to a minor extent.

A main feature of the EDX measurements of the anodes from the cells aged at 45 °C is the pronounced enrichment of F on the anode surface (Fig. 5e) and on the surfaces of the SiO_x particles (Figs. 5j,o,t). Figures 5j,o,t shows that F is also enriched on the graphite particle's surfaces, however, it is stronger for the SiO_x particles. In contrast, no such F enrichment is observed on the surfaces of the SiO_x particles in the anodes from the fresh cells (Figs. 3e, 3j) or in those aged at −10 °C (Figs. 4i, 4n). This is consistent with results on other cells by Feinauer et al.[36] and by Hsiao et al.[59] Aging at elevated temperature promotes the formation F-containing compounds e.g. from $LiPF_6$ decomposition[8,15,76] which are possibly those observed in Figs. 5j,o,t. This degradation of the SiO_x compound in the anode and the corresponding decrease of the N/P ratio is most likely the cause of the mechanism changes from BOL to MOL observed as shifts in the Arrhenius plots in Figs. 1b and 2b.

Conclusions

In this work, we addressed the question of time and temperature dependent degradation on the example of commercial 3.5 Ah Li-ion 18 650 cells with SiO_x/graphite anodes (∼2.5 wt.% Si) and Ni-rich NMC cathodes, which were systematically aged at 0.5 C and 0.85 C in the temperature range of −10 °C to +45 °C. The time and temperature dependent degradation is addressed using Arrhenius plots of aging rates on the cell level and FIB-SEM/EDX measurements in Post-Mortem analysis on the material level.

We show how and why Arrhenius plots of the aging rate change during aging from BOL (100%–95% SOH) to MOL (92.5%–87.5% SOH). The connection between Arrhenius plots derived from electrochemical aging data and Post-Mortem analysis reveals a direct mechanistic connection to LAAM by SiO_x degradation by complementary methods.

For BOL, the both, 0.5 C and 0.85 C lead to minima in the Arrhenius plots, which mark the transition temperatures of low and high temperature aging mechanisms of 15 °C and 19 °C, respectively. The minima in the Arrhenius plots are also interesting in particular as they represent the longest cycle life.

For aging at 0.5 C, the minimum in the Arrhenius plot shifts from 15 °C for BOL to 30 °C for MOL, indicating that the cells most likely get more prone to Li deposition. For 0.85 C, the minimum in the Arrhenius plot even vanished in the temperature range up to 45 °C for MOL, indicating that the effect is even stronger than at 0.5 C.

To gain more insights on the material changes during aging, Post-Mortem analysis with FIB-SEM/EDX mapping was carried out at BOL and MOL after cyclic aging at 0.85 C at −10 °C and 45 °C. FIB-SEM/EDX showed no changes of the SiO_x compound but an oxygen rich film at MOL after cyclic aging at −10 °C. In contrast, cyclic aging at 45 °C led to a film formation involving F on the surface of the SiO_x compound. This degradation of the SiO_x compound at 45 °C is most likely the cause for the anode areal capacity decrease observed earlier by Flügel et al.[47] for the same cell type resulting in a decrease of the N/P ratio and the observed changes in the Arrhenius plots after cycling in this study (see Figs. 1b and 2b).

Open remaining questions are how the nature of Si-based compound changes the extent of the N/P ratio decrease and how this could be prevented by material improvement or optimized operational conditions. Further work in this direction is ongoing in our labs.

Acknowledgments

The authors would like to thank A. Aracil-Regalado (ZSW) for cell disassembly. Additionally, financial support provided by the German Federal Ministry of Research, Technology and Space (BMFTR) within the HighSafe-3 project (03XP0568A) is gratefully acknowledged. This work contributes to the research performed at CELEST (Center for Electrochemical Energy Storage Ulm-Karlsruhe).

ORCID

Jihed Ayari https://orcid.org/0009-0004-4423-4578
Mintao Wan https://orcid.org/0000-0002-3502-9415
Dominic Bresser https://orcid.org/0000-0001-6429-6048
Thomas Waldmann https://orcid.org/0000-0003-3761-1668

References

1. M. Armand et al., *J. Power Sources*, **479**, 228708 (2020).
2. D. Aurbach, B. Markovsky, A. Rodkin, M. Cojocaru, E. Levi and H.-J. Kim, *Electrochim. Acta.*, **47**, 1899 (2002).
3. M. Wohlfahrt-Mehrens and T. Waldmann, *Encyclopedia of Electrochemical Power Sources*, Elsevier (2025). (available at: https://linkinghub.elsevier.com/retrieve/pii/B9780323960229003078).
4. M. Broussely, S. Herreyre, P. Biensan, P. Kasztejna, K. Nechev and R. J. Staniewicz, *J. Power Sources*, **97–98**, 13 (2001).
5. H. P. Lin, D. Chua, M. Salomon, H. C. Shiao, M. Hendrickson, E. Plichta and S. Slane, *Electrochem. Solid-State Lett.*, **4**, A71 (2001).
6. J. Vetter, P. Novák, M. R. Wagner, C. Veit, K. C. Möller, J. O. Besenhard, M. Winter, M. Wohlfahrt-Mehrens, C. Vogler and A. Hammouche, *J. Power Sources*, **147**, 269 (2005).
7. T. Waldmann, B. I. Hogg and M. Wohlfahrt-Mehrens, *J. Power Sources*, **384**, 107 (2018).
8. T. Waldmann, M. Wilka, M. Kasper, M. Fleischhammer and M. Wohlfahrt-Mehrens, *J. Power Sources*, **262**, 129 (2014).
9. I. Bloom et al., *J. Power Sources*, **111**, 152 (2002).
10. S. Käbitz, J. B. Gerschler, M. Ecker, Y. Yurdagel, B. Emmermacher, D. André, T. Mitsch and D. U. Sauer, *J. Power Sources*, **239**, 572 (2013).
11. M. Ecker, N. Nieto, S. Käbitz, J. Schmalstieg, H. Blanke, A. Warnecke and D. U. Sauer, *J. Power Sources*, **248**, 839 (2014).
12. B. Y. Liaw, E. P. Roth, R. G. Jungst, G. Nagasubramanian, H. L. Case and D. H. Doughty, *J. Power Sources*, **119–121**, 874 (2003).
13. M. Dubarry, B. Y. Liaw, M. S. Chen, S. S. Chyan, K. C. Han, W. T. Sie and S. H. Wu, *J. Power Sources*, **196**, 3420 (2011).
14. E. S. Zsoldos, D. T. Thompson, W. Black, S. M. Azam and J. R. Dahn, *J. Electrochem. Soc.*, **171**, 080527 (2024).
15. T. Waldmann, N. Ghanbari, M. Kasper and M. Wohlfahrt-Mehrens, *J. Electrochem. Soc.*, **162**, A1500–A5 (2015).
16. B. Stiaszny, J. C. Ziegler, E. E. Krauß, J. P. Schmidt and E. Ivers-tiffée, *J. Power Sources*, **251**, 439 (2014).
17. M. Börner, S. Klamor, B. Hoffmann, M. Schroeder, S. Nowak, A. Würsig, M. Winter and F. M. Schappacher, *J. Electrochem. Soc.*, **163**, A831–A7 (2016).
18. T. Waldmann, J. B. Quinn, K. Richter, M. Kasper, A. Tost, A. Klein and M. Wohlfahrt-Mehrens, *J. Electrochem. Soc.*, **164**, A3154–A62 (2017).
19. T. Waldmann, S. Gorse, T. Samtleben, G. Schneider, V. Knoblauch and M. Wohlfahrt-Mehrens, *J. Electrochem. Soc.*, **161**, A1742–A7 (2014).
20. S. Gorse, B. Kugler, T. Samtleben, T. Waldmann, M. Wohlfahrt-Mehrens, G. Schneider and V. Knoblauch, *Pract. Metallogr.*, **51**, 829 (2014).
21. T. Waldmann, R.-G. Scurtu, D. Brändle and M. Wohlfahrt-Mehrens, *Energy Technol.*, **11**, 2200583 (2022).
22. A. Pfrang, A. Kersys, A. Kriston, D. U. Sauer, C. Rahe, S. Käbitz and E. Figgemeier, *J. Power Sources*, **392**, 168 (2018).
23. L. Willenberg, P. Dechent, G. Fuchs, M. Teuber, M. Eckert, M. Graff, N. Kürten, D. U. Sauer and E. Figgemeier, *J. Electrochem. Soc.*, **167**, 120502 (2020).
24. J. E. Harlow et al., *J. Electrochem. Soc.*, **166**, A3031–A44 (2019).
25. J. Self, C. P. Aiken, R. Petibon and J. R. Dahn, *J. Electrochem. Soc.*, **162**, A796–A802 (2015).
26. V. Yufit, P. Shearing, R. W. Hamilton, P. D. Lee, M. Wu and N. P. Brandon, *Electrochem. Commun.*, **13**, 608 (2011).
27. A. Iturrondobeitia, F. Aguesse, S. Genies, T. Waldmann, M. Kasper, N. Ghanbari, M. Wohlfahrt-Mehrens and E. Bekaert, *J. Phys. Chem. C*, **121**, 21865 (2017).
28. J. C. Burns, A. Kassam, N. N. Sinha, L. E. Downie, L. Solnickova, B. M. Way and J. R. Dahn, *J. Electrochem. Soc.*, **160**, A1451–A6 (2013).
29. M. Bozorgchenani, G. Kucinskis, M. Wohlfahrt-Mehrens and T. Waldmann, *J. Electrochem. Soc.*, **169**, 030509 (2022).
30. G. Kucinskis, M. Bozorgchenani, M. Feinauer, M. Kasper, M. Wohlfahrt-Mehrens and T. Waldmann, *J. Power Sources*, **549**, 232129 (2022).
31. M. Feinauer, A. A. Abd-El-Latif, P. Sichler, A. A. Regalado, M. Wohlfahrt-Mehrens and T. Waldmann, *J. Power Sources*, **570**, 233046 (2023).
32. M. Feinauer, M. Wohlfahrt-Mehrens, M. Hölzle and T. Waldmann, *J. Power Sources*, **594**, 233948 (2024).
33. G. G. Gerosa, M. Feinauer, C. Hogrefe, S. Häfele, K. Bischof, M. Wörz, O. Böse, M. Wohlfahrt-Mehrens, M. Hölzle and T. Waldmann, *J. Electrochem. Soc.*, **172**, 030502 (2025).
34. N. Ghanbari, T. Waldmann, M. Kasper, P. Axmann and M. Wohlfahrt-Mehrens, *J. Phys. Chem. C*, **120**, 22225–34 (2016).
35. L. E. Downie, L. J. Krause, J. C. Burns, L. D. Jensen, V. L. Chevrier and J. R. Dahn, *J. Electrochem. Soc.*, **160**, A588–A94 (2013).
36. M. Feinauer, M. Wohlfahrt-Mehrens, M. Hölzle and T. Waldmann, *J. Electrochem. Soc.*, **171**, 110506 (2024).
37. T. Waldmann, M. Kasper and M. Wohlfahrt-Mehrens, *Electrochim. Acta.*, **178**, 525 (2015).
38. N. Ghanbari, T. Waldmann, M. Kasper, P. Axmann and M. Wohlfahrt-Mehrens, *ECS Electrochem. Lett.*, **4**, A100–A2 (2015).
39. T. Waldmann, B.-I. Hogg, M. Kasper, S. Grolleau, C. G. Couceiro, K. Trad, B. P. Matadi and M. Wohlfahrt-Mehrens, *J. Electrochem. Soc.*, **163**, A1232–A8 (2016).
40. P. Moosmann, J. Ayari, I. Jipa, M. Hölzle and T. Waldmann, *J. Electrochem. Soc.*, **172**, 080516 (2025).
41. K. Bischof, M. Flügel, M. Hölzle, M. Wohlfahrt-Mehrens and T. Waldmann, *J. Electrochem. Soc.*, **171**, 010510 (2024).
42. P. W. Atkins, J. de Paula and J. Keeler, *Atkins' Physical Chemistry*, Eleventh, p. 908, Oxford University (2018).
43. S. Azam, W. Black, H. MacLennan, A. Eldesoky and J. R. Dahn, *J. Electrochem. Soc.*, **172**, 020536 (2025).
44. M. Yue, M. D. Lumsden, J. Deshmukh, E. S. Zsoldos, W. Black, S. M. Azam and J. R. Dahn, *J. Electrochem. Soc.*, **172**, 050502 (2025).
45. B. P. Matadi et al., *J. Electrochem. Soc.*, **164**, A1089–A97 (2017).

46. B.-I. Hogg, T. Waldmann and M. Wohlfahrt-Mehrens, *J. Electrochem. Soc.*, **167**, 090525 (2020).
47. M. Flügel, K. Richter, M. Wohlfahrt-Mehrens and T. Waldmann, *J. Electrochem. Soc.*, **169**, 050533 (2022).
48. J. C. Burns, D. A. Stevens and J. R. Dahn, *J. Electrochem. Soc.*, **162**, A959–A64 (2015).
49. I. Pivarníková, M. Flügel, N. Paul, A. Cannavo, G. Ceccio, J. Vacík, P. Müller-buschbaum, M. Wohlfahrt-Mehrens, R. Gilles and T. Waldmann, *J. Power Sources*, **594**, 233972 (2024).
50. S. Hein and A. Latz, *Electrochim. Acta.*, **201**, 354 (2016).
51. N. Legrand, B. Knosp, P. Desprez, F. Lapicque and S. Raël, *J. Power Sources*, **245**, 208 (2014).
52. C. Hogrefe, M. Hölzle, M. Wohlfahrt-Mehrens and T. Waldmann, *J. Electrochem. Soc.*, **170**, 110535 (2023).
53. D. Stottmeister and A. Groß, *Batter. Supercaps*, **6**, e202300156 (2023).
54. M. Fleischhammer, T. Waldmann, G. Bisle, B.-I. Hogg and M. Wohlfahrt-Mehrens, *J. Power Sources*, **274**, 432 (2015).
55. T. Waldmann and M. Wohlfahrt-Mehrens, *Electrochim. Acta.*, **230**, 454 (2017).
56. P. Arora, M. Doyle and E. W. Ralph, *J. Electrochem. Soc.*, **146**, 3543 (1999).
57. T. Waldmann, A. Aracil-Regalado, K. Bischof, M. Wohlfahrt-Mehrens and M. Hölzle, *J. Electrochem. Soc.*, **172**, 100514 (2025).
58. X.-G. Yang and C.-Y. Wang, *J. Power Sources*, **402**, 489 (2018).
59. H.-C. Hsiao, A. Adam, D. Goldbach, Y. Dai, J. Li, T. Waldmann and M. Hölzle, *J. Electrochem. Soc.*, **172**, 070534 (2025).
60. I. Zilberman, J. Sturm and A. Jossen, *J. Power Sources*, **425**, 217 (2019).
61. T. Waldmann et al., *J. Electrochem. Soc.*, **171**, 070526 (2024).
62. R. V. Feser, A. A. Abd-El-Latif, I. Jipa, M. Hölzle and T. Waldmann, *J. Electrochem. Soc.*, **172**, 090501 (2025).
63. J. Wu, Y. Cao, H. Zhao, J. Mao and Z. Guo, *Carbon Energy*, **1**, 57 (2019).
64. E. Peled and S. Menkin, *J. Electrochem. Soc.*, **164**, A1703–A19 (2017).
65. K. Edström, M. Herstedt and D. P. Abraham, *J. Power Sources*, **153**, 380 (2006).
66. K. Richter, T. Waldmann, M. Memm, M. Kasper and M. Wohlfahrt-Mehrens, *J. Electrochem. Soc.*, **165**, A3602–A4 (2018).
67. K. Richter, T. Waldmann, M. Kasper, C. Pfeifer, M. Memm, P. Axmann and M. Wohlfahrt-Mehrens, *J. Phys. Chem. C*, **123**, 18795 (2019).
68. K. Richter, T. Waldmann, N. Paul, N. Jobst, R. Scurtu, M. Hofmann, R. Gilles and M. Wohlfahrt Mehrens, *Chem. Sus. Chem.*, **13**, 529 (2020).
69. F. Allgayer, M. H. Hofmann, H. Ehrenberg, M. Storch and F. Jeschull, *J. Power Sources*, **665**, 239053 (2026).
70. Z. Zeng, W.-I. Liang, H.-G. Liao, H. L. Xin, Y.-H. Chu and H. Zheng, *Nano Lett.*, **14**, 1745 (2014).
71. M. Flügel, M. Bolsinger, M. Marinaro, V. Knoblauch, M. Hölzle, M. Wohlfahrt-Mehrens and T. Waldmann, *J. Electrochem. Soc.*, **170**, 060536 (2023).
72. C. Hogrefe, T. Waldmann, M. Hölzle and M. Wohlfahrt-Mehrens, *J. Power Sources*, **556**, 232391 (2023).
73. L. Boveleth, A. Lindner, W. Menesklou, T. Danner and A. Latz, *Electrochim. Acta.*, **506**, 145010 (2024).
74. Y.-C. Hsieh, M. Leißing, S. Nowak, B.-J. Hwang, M. Winter and G. Brunklaus, *Cell Rep. Phys. Sci*, **1**, 100139 (2020).
75. K. Jalkanen, J. Karppinen, L. Skogström, T. Laurila, M. Nisula and K. Vuorilehto, *Appl. Energy*, **154**, 160 (2015).
76. D. Aurbach, B. Markovsky, A. Shechter, Y. Ein-eli and H. Cohen, *J. Electrochem. Soc.*, **143**, 3809 (1996).